

Galaxy cluster mass estimation with deep learning and hydrodynamical simulations

Z. Yan,^{1*} A. J. Mead,^{1,3} L. Van Waerbeke,¹ G. Hinshaw,¹ I. G. McCarthy²

¹*Department of Physics and Astronomy, University of British Columbia, 6224 Agricultural Road, Vancouver, BC, V6T 1Z1, Canada*

²*Astrophysics Research Institute, Liverpool John Moores University, 146 Brownlow Hill, Liverpool, L3 5RF, UK*

³*Institut de Ciències del Cosmos, Universitat de Barcelona, Martí Franquès 1, E-08028 Barcelona, Spain*

Accepted XXX. Received YYY; in original form ZZZ

ABSTRACT

We evaluate the ability of Convolutional Neural Networks (CNNs) to predict galaxy cluster masses in the BAHAMAS hydrodynamical simulations. We train four separate single-channel networks using: stellar mass, soft X-ray flux, bolometric X-ray flux, and the Compton y parameter as observational tracers, respectively. Our training set consists of ~ 6400 synthetic cluster images generated from the simulation, while an additional ~ 1600 images form a test set. We also train a ‘multi-channel’ CNN by combining the four observational tracers. We utilize `keras` with a `Tensorflow` backend to train the network, and all four converge within 2000 epochs. The cluster masses predicted from these networks are evaluated using the average fractional difference between predicted cluster mass and true cluster mass. The resulting predictions are especially precise for halo masses in the range $10^{13.25} M_{\odot} < M < 10^{14.5} M_{\odot}$, where all five networks produce mean mass biases of order $\approx 1\%$ with a scatter on the mean bias of $\approx 0.5\%$. The network trained with Compton y parameter maps yields the most precise predictions. We interpret the network’s behaviour using two diagnostic tests to determine which features are used to predict cluster mass. The CNN trained with stellar mass images detect galaxies (not surprisingly), while CNNs trained with gas-based tracers utilise the shape of the signal to estimate cluster mass.

Key words: hydrodynamics – methods: convolutional neural network – galaxies: clusters: general – galaxies: groups: general – dark matter – large-scale structure of Universe

1 INTRODUCTION

Galaxy groups and clusters are collections of several up to thousands of galaxies that are bound by their mutual gravity. With masses in the range of 10^{13} – $10^{15} M_{\odot}$, they are the most massive collapsed objects in the Universe. Their abundance, distribution, and morphology depends both on local physical processes and the underlying cosmological model. Stars typically comprise about 1% of a cluster’s mass (e.g., Leauthaud et al. 2011; Zu & Mandelbaum 2015), while hot gas contributes anywhere from ≈ 7 –13% (depending on cluster mass; e.g., Allen et al. 2002; Sun et al. 2009; Pratt et al. 2009), with the remainder residing in a dark matter halo.

The cluster mass function is a particularly sensitive probe of cosmological parameters and the evolutionary history of large-scale structure (e.g. Voit 2005; Allen et al. 2011; Planck Collaboration et al. 2016). However, it is diffi-

cult to precisely and accurately measure cluster masses directly because they are dominated by dark matter. Masses can be inferred from weak gravitational lensing data (e.g. Umetsu 2010; Shan et al. 2012; Hoekstra et al. 2015; von der Linden et al. 2014), but the current signal-to-noise ratio of such observations limits the precision of individual cluster masses to typically (at least) tens of percent. This is not sufficiently precise to be used directly for precision cosmology (via the mass function), but weak lensing is still a very important probe because it can be used to calibrate the mean bias¹ of other tracers whose system-to-system scatter is lower. Examples of such tracers include the total stellar mass or cluster richness, X-ray emission in the form of thermal bremsstrahlung and recombination lines from the

¹ It has been shown from mock analyses of weak lensing observations of simulated clusters that weak lensing mass measurements yield a nearly unbiased mean mass estimate (e.g., Becker & Kravtsov 2011; Bahé et al. 2012).

* E-mail: yanza15@phas.ubc.ca

hot intracluster medium (ICM), and the thermal Sunyaev-Zel'dovich effect (i.e., the inverse Compton scattering of cosmic microwave background photons off hot ICM electrons as they pass through clusters).

Note that X-ray emission itself can be used to infer mass by combining spectroscopic measurements of the temperature profile with surface brightness measurements that strongly constrain the density profile, allowing one to infer a mass under the assumption of hydrostatic equilibrium. How well this assumption holds is currently a subject of strong debate, with the level of deviation from hydrostatic equilibrium having been estimated to be anywhere from 40% (i.e., the hydrostatic mass underestimates the true mass by this amount; e.g., von der Linden et al. 2014) to only $\lesssim 5\%$ (e.g., Melin & Bartlett 2015; Smith et al. 2016).

Large-scale hydrodynamical simulations are playing an increasingly important role in calibrating the inference of cluster masses from observational data. These simulations are now capable of capturing gravitational and gas dynamics on cosmological scales and can therefore provide large samples of realistic clusters in order to assess mass inferences statistically. They also aid in understanding systematic effects that may hinder these inferences (see Borgani & Kravtsov 2011 for a review of hydrodynamical simulations). However, even with these simulations, the complexities of substructure, morphology and small-scale physical processes, such as AGN feedback (Gitti et al. 2012) and gas clumping (Nagai & Lau 2011), hinder the accuracy of many cluster mass estimates. Yan et al. (2020) used hydrodynamical simulations to assess the effect of cluster mis-centering on mass determinations.

Machine learning (ML) is a technique in which computer systems learn to analyze data without using explicit instructions or model parameterisations, but instead are ‘trained’ to make decisions based on properties of the data itself. In astronomy, ML algorithms such as linear regression, decision tree, random forest and Principal Component Analysis have been widely used in model fitting and feature extraction (see Baron (2019) for a review).

Artificial Neural Networks (ANNs) are a popular class of ML tools inspired by the way in which biological nervous systems, such as the brain, process information. ANNs use a hierarchy of simple functions, called activation functions, to construct a highly nonlinear function. Given their ability to mimic complicated functions, ANNs form the basis of many voice recognition and image identification tools. A Convolutional Neural Network (CNN) is a category of ANN that is particularly useful in the field of object identification and image classification. CNNs have been used by astronomers to classify galaxy morphology (Banerji et al. 2010), to identify lensing shear (Lanusse et al. 2017), to generate cosmic webs (Rodríguez et al. 2018), and to directly constrain cosmological parameters (Ribli et al. 2019).

Cohn & Battaglia (2019) used multiple machine-learning algorithms to estimate cluster mass from a set of observable quantities. Ntampaka et al. (2018) trained a CNN to predict cluster mass from mock X-ray images. Here we extend their work and utilize CNNs to predict cluster masses from stellar mass data, X-ray data, Compton y data, and from combinations of them. The test data are the BAHAMAS hydrodynamical simulations (McCarthy et al. 2017). We choose M_{200} as the proxy for cluster mass. This

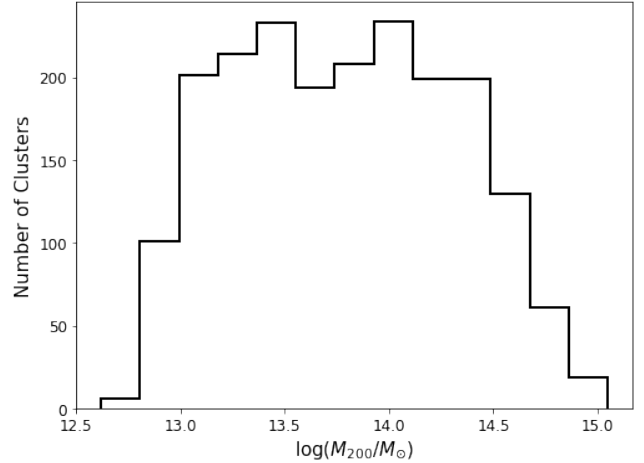


Figure 1. The mass distribution of galaxy clusters that we analyze from the BAHAMAS simulation.

is the total mass within the characteristic radius r_{200} , the radius at which the cluster density falls to 200 times the critical density of the (simulated) universe.

The structure of this paper is as follows: §2 describes the simulation data and the setup of our CNN; §3 presents our results; §4 describes a test to understand the behaviour of the CNN; and §5 presents our conclusions.

2 DATA AND METHOD

2.1 The BAHAMAS Simulation

We employ data from the BAHAMAS (BArions and Haloes of MAssive Systems, McCarthy et al. 2017, 2018) simulations. BAHAMAS is a suite of cosmological, hydrodynamical simulations run using a modified version of the TreePM SPH code **GADGET3**. The simulations consist of 400 cMpc/h periodic boxes containing 2×10^{14} particles (with equal numbers of dark matter and baryonic particles). The run we use adopts the WMAP 9-year best-fit cosmology with massless neutrinos (Hinshaw et al. 2013).

BAHAMAS includes subgrid treatments of important physical processes that cannot be directly resolved in the simulations, including metal-dependent radiative cooling, star formation, stellar evolution and mass-loss, black hole formation and growth, and stellar and active galactic nuclei (AGN) feedback. The subgrid models were developed as part of the OWLS project (Schaye et al. 2010). The parameters governing the efficiencies of AGN and stellar feedback were adjusted so that the simulations approximately reproduce the observed galaxy stellar mass function for $M_{*} \geq 10^{10} M_{\odot}$ and the hot gas fraction–halo mass relation of groups and clusters, as determined from high-resolution X-ray observations of local systems. As shown in McCarthy et al. (2017), the simulations match the galaxy–halo–tSZ–X-ray scaling relations of galaxies and groups and clusters.

For the present study, friends-of-friends (FoF) halos are selected from the dark-matter-only simulation that accom-

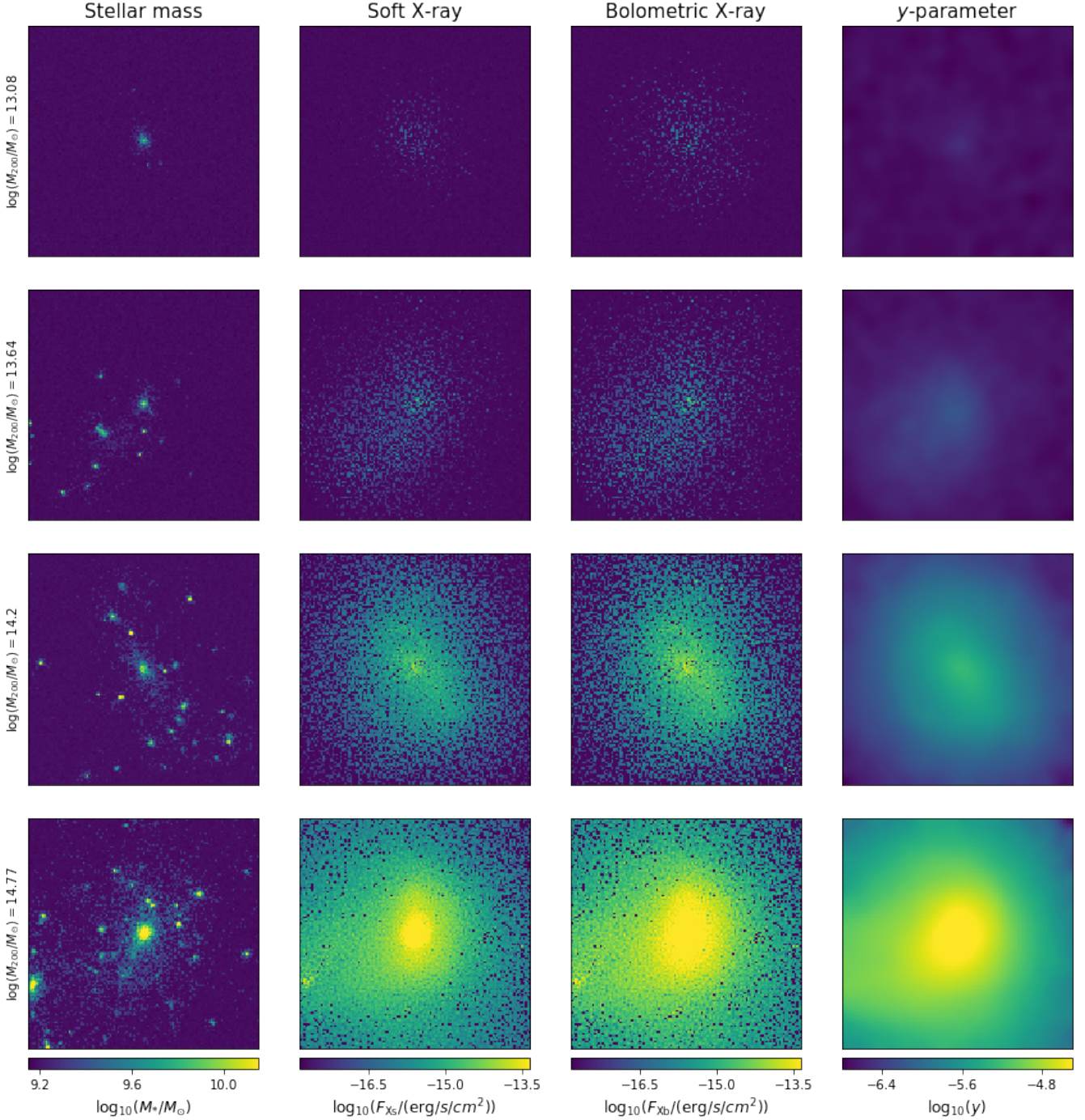


Figure 2. Selected cluster images from the BAHAMAS simulation. Each row is a cluster drawn from a different mass range, as indicated, and each column is a different observable: stellar density, soft X-ray luminosity, bolometric X-ray luminosity, and Compton y parameter. The colour scales are the same across the mass range (rows). The angular size of all the image are 20 arcmin.

panies the BAHAMAS hydrodynamical simulations². We select up to 200 halos in each of 10 mass bins of width of 0.25 dex, spanning the range $M_{200} = 10^{13} - 10^{15} M_{\odot}$, resulting in a sample of almost 2000 halos (some bins have slightly

² We select halos from a dark matter-only simulation so as to facilitate comparisons with hydrodynamical runs that vary feedback and the cosmological model.

fewer than 200 halos). This sample is then matched to the BAHAMAS hydrodynamical simulation. The resulting number distribution of clusters as a function of mass is shown in Fig. 1. The distribution is not perfectly flat because the hydrodynamical masses are different from the underlying dark-matter-only masses.

We tag all particles (gas, dark matter, and stellar) within $2r_{200}$ of the most bound particle (MBP) for analy-

sis. We also generate a catalog of simulated galaxies within this radius that have $M_{\text{gal}} > 10^{10} M_{\odot}$. (Simulated galaxies are defined as the stellar component of self-gravitating substructures identified with the SUBFIND algorithm.)

The soft and bolometric X-ray luminosity of each gas particle is provided with the simulation. For the tSZ signal, a quantity Υ is calculated for each gas particle (McCarthy et al. 2018),

$$\Upsilon \equiv \sigma_T \frac{k_B T}{m_e c^2} \frac{m}{\mu_e m_H}, \quad (1)$$

where T is the gas particle's temperature, m is the gas particle's mass, μ_e is the mean molecular weight per free electron of each gas particle, and m_H is the atomic mass of hydrogen.

2.2 Data set and image generation

The data sets used to train the neural networks are images of each of the four observables derived from the simulated cluster sample. The cluster catalog contains ~ 2000 clusters, but this is insufficient to train the neural network to the desired level of precision. To overcome this, we generate 3 additional copies of each cluster by rotating them in 3-D by $\pi/2$ about the x and y axis, and by a random angle between $\pi/6$ and $\pi/3$ about the x axis. The simulated clusters are provided at redshift 0, but we place them at random redshifts between 0.03 and 0.07 (with a uniform distribution) when we produce images. In the end, we have ~ 8000 clusters at different redshifts with which to train the neural networks.

The image of each cluster is made by projecting it onto the x - y plane and binning the particles onto an 120×120 grid with an overall angular size of 20 arcmin. For a cluster at redshift z , the signal in pixel (i, j) for each observable is obtained as follows.

Stellar density - We evaluate the stellar surface density in each pixel as

$$I_{ij} = \sum_{p \in (i,j)} M_s(\mathbf{r}_p)/S, \quad (2)$$

where the sum is over all stellar particles that project into pixel (i, j) , $M_s(\mathbf{r}_p)$ is the stellar mass of particle p (located at position \mathbf{r}_p with respect to the cluster centre), and S is the physical area of pixel (i, j) . The angular coordinates of pixel (i, j) are

$$\theta_p = (x_p, y_p)/d_A(z), \quad (3)$$

where (x_p, y_p) are the x and y components of \mathbf{r}_p and $d_A(z)$ is the angular diameter distance to redshift z .

X-ray emission - We convert luminosity into flux using $F = L/4\pi d_L(z)$, where $d_L(z)$ is the luminosity distance to redshift z . The signal in pixel (i, j) is the flux due to all gas particles that project into that pixel,

$$I_{ij} = \sum_{p \in (i,j)} F(\mathbf{r}_p) = \sum_{p \in (i,j)} \frac{L(\mathbf{r}_p)}{4\pi d_L(z)}. \quad (4)$$

Compton y parameter - The signal in pixel (i, j) is obtained by summing Υ/S (McCarthy et al. 2018) over all gas particles that project into that pixel,

$$I_{ij} = \sum_{p \in (i,j)} \Upsilon(\mathbf{r}_p)/S. \quad (5)$$

Signal	Label	Units	Noise [rms]	Beam [FWHM]
Stellar Mass	Star	M_{\odot}	2.14×10^{11}	-
Soft X-ray	Fxs	erg/s/cm ²	9×10^{-16}	4''
Bolometric X-ray	Fxb	erg/s/cm ²	9×10^{-16}	4''
Compton y	Ypar	-	10^{-8}	1.4'

Table 1. Simulated data set properties. The labels are used throughout this paper.

For low-mass clusters (those with $2\theta_{200} < 20'$), all cluster particles reside within the image, while for high-mass clusters, some particles extend outside the image and are lost. Our choice of image size strikes a balance between performance and computation time.

In order to mimic realistic data, we add noise to our images and smooth them to mimic a telescope point spread function (PSF). For stellar images, we take the rms to be 1/10 the mean mass across the whole sample giving a signal-to-noise-ratio roughly 10, which mimics an SDSS-like observation (Abazajian et al. 2009). No smoothing is applied since most optical telescopes have a beam size smaller than our pixel size. The gas-based images have Gaussian random noise added and are then smoothed with a Gaussian beam. For the X-ray images, the rms noise and beam size are chosen to match the Chandra HRI sensitivity and FWHM, respectively (Abazajian, Adelman-McCarthy, Agüeros, Allam, Prieto, An, Anderson, Anderson, Annis, Bahcall et al. cha). For the Compton y image, the rms noise is taken to be 10^{-8} per pixel and the beam FWHM is 1.4 arcmin, corresponding to an ACT-like experiment (Hasselfield et al. 2013). We have also considered a *Planck*-like experiment with rms noise 10^{-6} and a FWHM of 9.66 arcmin (Aghanim et al. 2016), but the CNN to performed quite poorly in this case. The parameters discussed above are summarized in Table 1. Images of each observable, in four clusters selected to have different masses, are shown in Fig. 2.

2.3 Artificial Neural Network

An Artificial Neural Network (ANN) is a function which maps inputs to outputs,

$$\text{ANN}(I) = O, \quad (6)$$

where I is the input and O is the output. In practice, the inputs can be images, sounds, text, etc., and the output can be a parameter to measure, a classification, and so on. A typical ANN is a sequential nest of functions that are defined on each layer of the network. In the simplest case of a feed-forward neural network, the neuron layers are evaluated in sequence, passing information from layer to layer. The output, a_k^l , of the k -th neuron in the l -th layer may be written as

$$a_k^l = f \left(\sum_j W_{jk}^l a_j^{l-1} + b_k^l \right), \quad (7)$$

where f is called an activation function (our choice of f is defined in the following section), W_{jk}^l is a matrix of weights, and b_k^l is a vector of additive biases. a_k^0 is the input

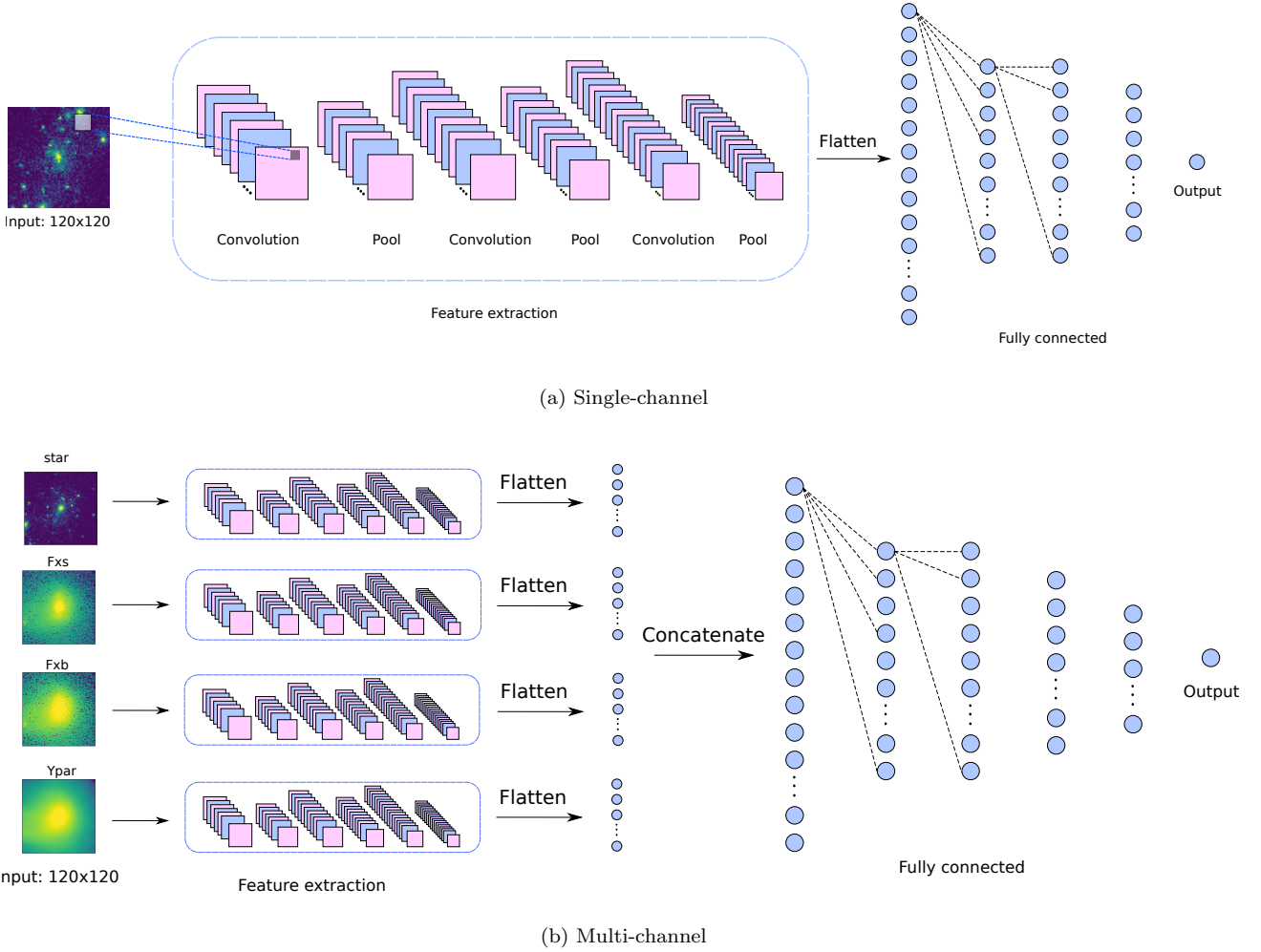


Figure 3. Upper panel: Architecture of the single-channel CNN used in this analysis. Our network utilizes three convolutional and pooling layers for feature extraction and four fully connected layers for parameter estimation. Lower panel: Architecture of the multi-channel CNN. The four channels take images: Star, Fxs, Fxb, and Ypar, respectively and perform feature extraction independently. The feature extraction layers have the same structure as the single-channel portion outlined in the upper panel.

data, I , and a in the last layer is the output, O . Schematically, W_{jk}^l connects the j -th neuron in layer $(l-1)$ to the k -th neuron in layer l . The number of neurons and layers, or equivalently, the dimensions of W_{jk}^l and b_k^l are called the architecture of the ANN. Given the architecture and activation functions, the ANN is completely specified W_{jk}^l and b_k^l .

ANN training is a fitting procedure to determine the parameters W and b required to reproduce known information (so-called ‘labels’) from data. The labels can be categories (for a classification task) or quantities (for a measurement task), and so on. For example, an ANN designed to recognise hand-written numbers is a classifier that takes hand-written images of numbers as input, and generates numbers as output labels.

ANN training involves iteratively optimizing the weights so as to minimize the difference between the output labels and the known labels, as quantified by the loss function. The ANN is initialized with random weights and biases, then, during each iteration (‘epoch’), the training data is provided to the ANN and outputs are predicted from

them. The weights and biases are updated to reduce the loss function by an algorithm called an optimizer. The training is complete when the loss function converges. To validate the process, a ‘test set’ (whose labels are also known) is then supplied to the ANN. If the ANN gives accurate predictions for the test set, then one can safely use it to predict labels from data whose labels are not known.

2.4 Convolutional Neural Network

In our analysis we use a category of ANN called a Convolutional Neural Network (CNN). The typical input of a CNN is a two-dimensional image, and the CNN uses convolution layers to extract features from them (for example, textures, edges, gradual changes and so on). Unlike fully-connected layers, in which each neuron is connected to each of the previous neurons, convolutional layers pass forward information from a small neighborhood around each neuron. A convolution layer is comprised of several $n \times n$ filters, where n is smaller than the input image dimension. The filtered image

is given by

$$I_{ij}^F = \sum_{i'j'} F_{i'j'} I_{i+i', j+j'}, \quad (8)$$

where the sum runs over the $n \times n$ set of filter pixels, centred on $(i', j') = (0, 0)$. The output is called a feature image, and within the same convolutional layer, different filters extract different kinds of features (for example, horizontal and vertical textures). The parameters in a filter define a set of weights that are optimized during training. The feature images are downsized into a ‘pooling layer’, so the feature images get smaller as they pass through convolution-pooling layers. Different convolution layers can be designed to extract information on different scales by tuning the filter size, n , and the feature image size. In our analysis, n is fixed to 3. The pooling filter is 2×2 with a stride of 2 pixels. This means that each pixel in the pooling layer is the average of a 2×2 patch in the previous feature image with a stride of 2 pixels. This process is called ‘average pooling’, which downsizes the feature image by a factor of 2. As the feature images are downsized from layer to layer, the deeper convolution layers extract larger scale features. By using convolution and pooling layers, one can also reduce the computational cost and make the result easier to interpret. A sequence of convolution-pooling layers is flattened into a one-dimensional layer followed by fully connected layers to further parameterize the features.

In our application, we utilize a CNN to predict cluster masses, so the output layer is a single neuron: the cluster mass. In the training set, we label each cluster with the M_{200} value calculated by summing the masses of all simulated particles within r_{200} of the cluster centre. In the rest of this paper, we denote this value as M_{true} , and we denote the CNN-predicted mass by M_{pred} . For each training run, we randomly select 80% of our 120×120 images as the training set and the remaining 20% as the test set.

We train the four ‘single-channel’ CNNs with the four data sets described in Table 1. We can write

$$\text{CNN}^c(I_{ij}^c) = M_{\text{pred}} \quad (9)$$

where I_{ij}^c is the image of tracer $c \in \{\text{Star}, \text{Fxs}, \text{Fxb}, \text{Ypar}\}$, (i, j) is the 2-D pixel index, and M_{pred} is the predicted M_{200} . To assess the advantage of multiple tracers, we also train a ‘multi-channel’ CNN, denoted CNN^{mc} , by simultaneously feeding all four data sets into one neural network,

$$\text{CNN}^{mc}(I_{ij}^{\text{Star}}, I_{ij}^{\text{Fxs}}, I_{ij}^{\text{Fxb}}, I_{ij}^{\text{Ypar}}) = M_{\text{pred}}. \quad (10)$$

For each layer except the output layer, we use the Rectified Linear Unit (ReLU) as our activation function. This is defined as $f(x) \equiv \max\{0, x\}$. To prevent over-fitting, we force a 20% dropout between fully-connected layers, which means that, for each training epoch, 20% of the weights (randomly selected) between those layers are set to zero. A dropout fraction slows down the training, so we chose this value to prevent over-fitting while keep the training fairly fast. For the output layer, we use the mean-squared-logarithmic-error as our loss function, defined as

$$\delta \equiv \left\langle \left(\log M_{\text{pred}} - \log M_{\text{true}} \right)^2 \right\rangle. \quad (11)$$

During training, the loss function of the test set (the so-called validation loss) is calculated in each epoch to monitor

the progress of the training. Our convergence criterion is discussed below.

Our CNN is implemented using the **keras** package with a **Tensorflow** back-end written in **python**. Our network architecture is similar to that used by Ntampaka et al. (2018), which is a simplified version of that used by Simonyan & Zisserman (2014):

1. 3×3 convolution with 16 filters
2. 2×2 , stride-2 average pooling
3. 3×3 convolution with 32 filters
4. 2×2 , stride-2 average pooling
5. 3×3 convolution with 64 filters
6. 2×2 , stride-2 average pooling
7. Flatten
8. Fully-connected with 200 neurons
9. 10% dropout
10. Fully-connected with 100 neurons
11. 10% dropout
12. Fully-connected with 100 neurons
13. 10% dropout
14. Fully-connected with 20 neurons
15. Output neuron

For our multi-channel network, each data channel is convolved, pooled, and flattened separately, using the same architecture as the single-channel network. As shown in Fig. 3b, the flattened layers from each channel are concatenated into one flattened layer, followed by fully-connected layers with the same architecture as the single-channel network.

We use **RMSprop** (Hinton et al. 2012) as our optimizer because it converges quickly in this application. We set the learning rate (the step size in the parameter space) to be 0.01 with decay rate of 10^{-4} . We tested other combinations of optimizers and learning rates, but this choice gave the best performance. The training data is divided into batches of 50 images each. In one training epoch, the network is trained through each batch separately, and the CNN weights are obtained by averaging over all batches. Each network was trained for 1000 epochs on 2 GPUs with 6 CPUs. The training took about 20 minutes for a single-channel network, and 45 minutes for the multi channel network.

Fig. 4 shows the ‘learning curve’ (the loss function of the test set as a function of training epoch) for each of our CNNs. During training, the test loss drops quickly at first, then converges after ~ 600 epochs. The final CNN weights are taken to be those which gave the minimum test loss during training.

3 RESULTS

Our cluster mass predictions are shown in Fig. 5. For each cluster in the test set, we show the CNN-predicted mass versus the true M_{200} measured in the simulation. In this rendition, all five data sets produce similar results. Fig. 6 shows the fractional mass bias for each tracer as a function of the true mass. The CNN generally *over*-predicts the mass by $\sim 15\%$ in the lowest mass bin, while it *under*-predicts the mass by $\sim 10\%$ in the highest mass bin. We attribute this edge effect to the mass cut in the prior distribution of true cluster masses available during training.

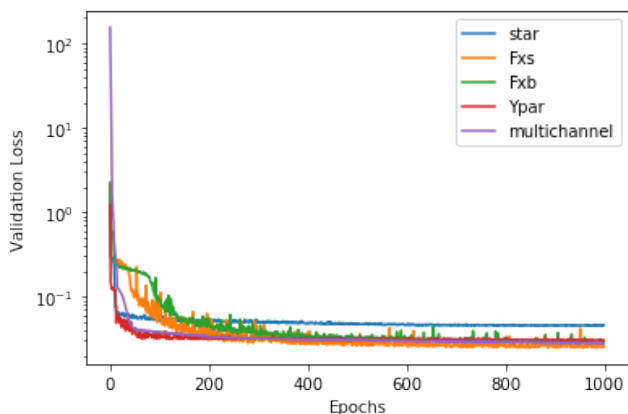


Figure 4. The learning curves for each of our five CNNs as a function of training epoch. The y-axis is the validation loss function defined in equation (11).

Signal	$\log \frac{M_{\text{pred}}}{M_{\text{true}}}$	$\frac{\Delta M}{M_{\text{true}}} (\%)$	$rms (\%)$
Star	-0.017 ± 0.003	-1.961 ± 0.626	18.989
Fxs	-0.014 ± 0.002	-2.370 ± 0.434	13.072
Fxb	-0.009 ± 0.002	-1.031 ± 0.487	14.588
Ypar	0.005 ± 0.002	2.206 ± 0.506	15.615
Multi-channel	0.002 ± 0.002	1.502 ± 0.490	14.948

Table 2. The mass bias ($\Delta M \equiv M_{\text{pred}} - M_{\text{true}}$) and scatter obtained from the test set for $13.25 < \log(M_{200,\text{true}}/M_{\odot}) < 14.5$.

Within the central mass range of $13.25 < \log(M_{200,\text{true}}/M_{\odot}) < 14.5$ (the shaded region in Fig. 6), the mass bias is quite small. Histograms of the mass bias in these central bins are shown in Fig. 7. Each tracer is plotted as a separate colour, with the gas-based tracers plotted as dashed curves, for clarity. A summary of our numerical results, both the average bias and the *rms* scatter, are given in Table 2.

The average mass bias, $\Delta M/M_{\text{true}}$, in the central mass bins is on the order of 1% with an uncertainty of $\sim 0.5\%$. The uncertainty per individual cluster is of order 15% (Table 2). Somewhat surprisingly, the multi-channel network is not the most precise. We assume this is due to limitations in the CNN architecture to synthesize information across all 4 tracers.

Henson et al. (2016) evaluate the performance of conventional mass estimation techniques applied to the BAHAMAS hydrodynamical simulations. They fit cluster lensing profiles with both NFW and Einasto models and are able predict masses with a bias of $\Delta M/M_{\text{true}} = -8.9^{+0.3}_{-0.2}\%$, and $-6.4^{+0.3}_{-0.2}\%$, respectively. Their analysis is based on weak lensing profiles which bear richer information about cluster masses. However, they don't include observational effects such as noise and smoothing. Yan et al. (2020) analyze the same BAHAMAS catalog by fitting an NFW model to the density profile of all particles in a cluster and infer a mean mass bias of roughly -10% . We conclude that our CNN-based results are more accurate than these profile-based analyses performed on the same hydrodynamical simulation, possibly due to limitations in the profile models.

As a reference to real observation, Zhang et al. (2008) use scale relations of X-ray observations to evaluate real cluster masses and get an individual mass uncertainty of $\sim 30\%$; Bleem et al. (2015) also use scale relation of tSZ signal to estimate mass for SPT galaxy clusters and get a mass uncertainty of $\sim 24\%$ for each cluster. Hoekstra et al. (2015) use weak lensing techniques to evaluate the masses of clusters. They estimate an uncertainty of about 20% which, if correct, indicates that the precision of our CNN-based method is not significantly better than weak lensing analysis. However, the weak lensing analysis is generally performed on more massive clusters which are not readily available in our simulation, so the comparison is not completely apt.

We test the sensitivity of our already-trained CNN to noise by varying the noise level of the tracer data in the test set between 0 and 4 times the fiducial levels given in Table 1. The bias in predicted mass from these altered test sets is still very small, so we conclude that the CNN is not overly sensitive to errors in the assumed noise level.

4 INTERPRETING THE CNN PERFORMANCE

Cluster masses are traditionally estimated using scaling relations based on known physics. For example, in relaxed clusters, X-ray luminosity is related to cluster mass via the virial theorem. In contrast, neural networks contain a large number of parameters, which makes their behaviour difficult to interpret. What makes the network predict a particular value of mass? What cluster feature(s) is it sensitive to? In this section, we attempt to interpret our single-channel networks in two ways.

Deep Dream: Google's Deep Dream (DD) (Mordvintsev et al. 2015) is an iterative, gradient ascent algorithm that is applied to an input image to determine which image pixels affect a particular output neuron the most. In our application, we have one output neuron, M_{pred} , so DD may be expressed in the form

$$I_{ij}^{(p)} = I_{ij}^{(p-1)} + \alpha \frac{\partial M_{\text{pred}}}{\partial I_{ij}} \bigg|_{I^{(p-1)}}, \quad (12)$$

where $I_{ij}^{(p)}$ is the image at the p -th iteration of the algorithm, and α is the step size. For small α , the difference between successive image iterations is proportional to the gradient of M_{pred} with respect to the image.

We ran 1 iteration of DD for each data tracer, selecting images from a range of true cluster masses. (We also ran 2 iterations, as did Ntampaka et al. (2018), and found similar results.) The gradient images for these examples are shown in the middle columns of Figures 8–11. In the stellar mass examples, the pixels that affect the predicted mass the most (rendered in yellow) appear to lie mostly *adjacent* to the galaxy locations. This suggests that CNN^{star} is mainly triggering on the number and size of galaxies in the image.

The gas-based tracers are more diffuse and symmetric, and this is reflected in the DD gradient images. For the X-ray tracers, the gradient images are quite granular, reflecting the granularity of the input images. But the critical information captured by the CNNs appears to be the shape of a cluster. For example, in the bottom row of Fig. 9, we see that the Fxs image has substructure at the top-left,

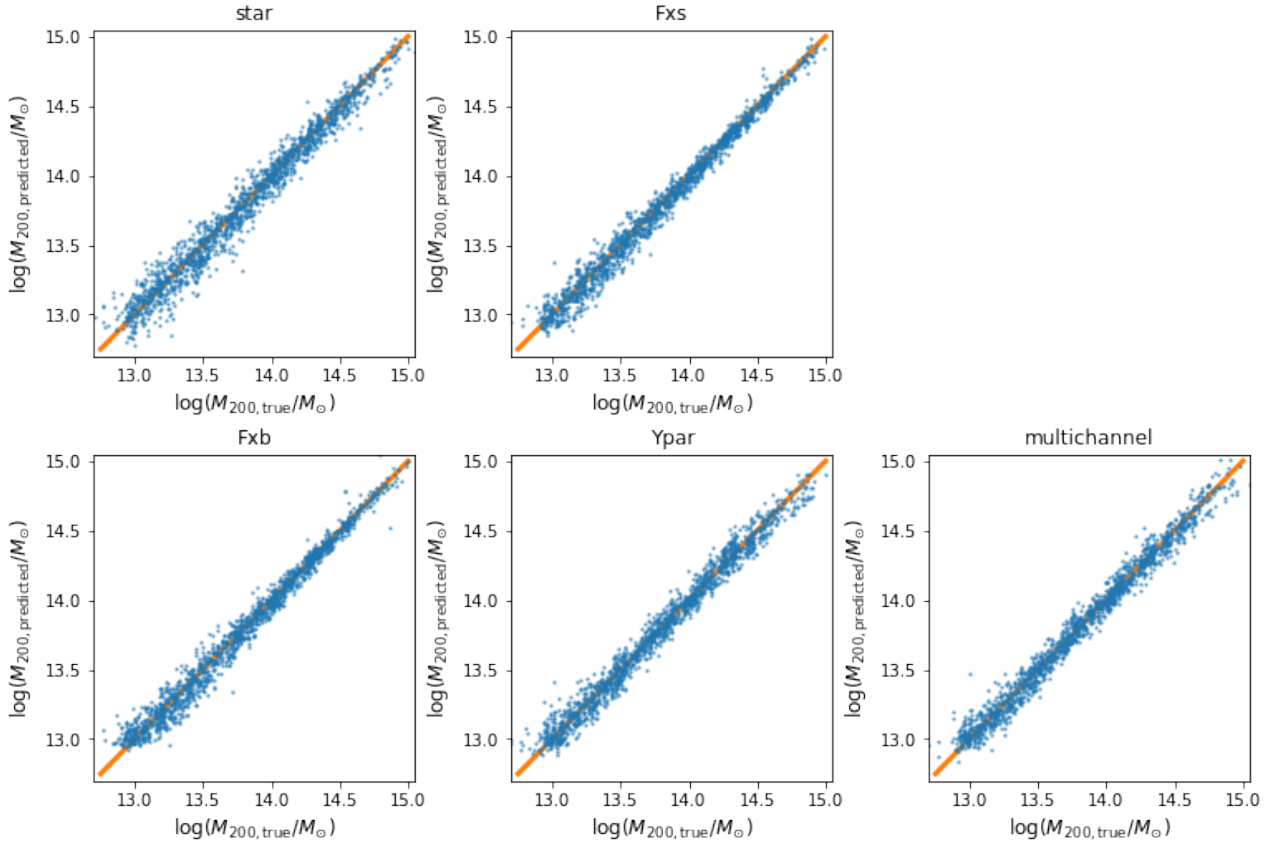


Figure 5. The CNN-predicted cluster mass vs. the true mass for each cluster in the test set. Each tracer is shown separately, for clarity.

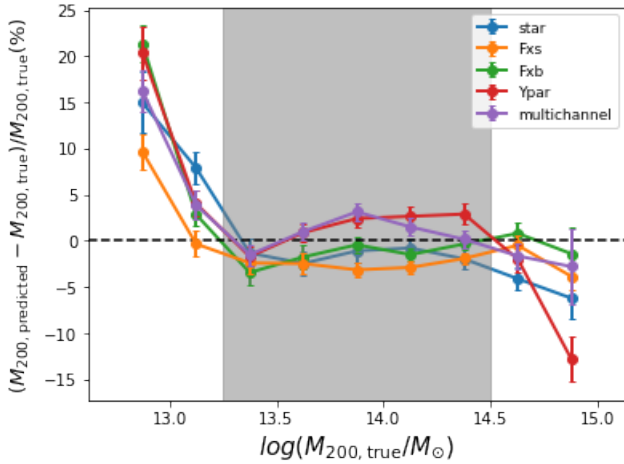


Figure 6. The bias in our CNN-predicted cluster masses as a function of the true mass, for each tracer. The plotted uncertainties show the standard deviation of the bias in each bin. The bias is small within the central mass range of $13.25 < \log(M_{200, \text{true}}/M_{\odot}) < 14.5$ (the shaded region).

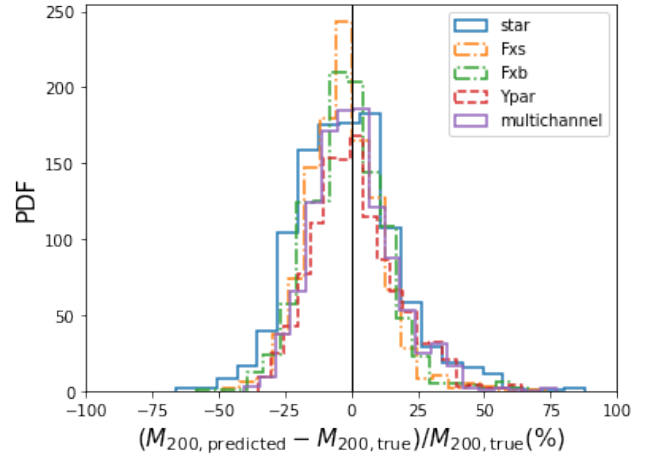


Figure 7. The probability distribution of the mass bias for each tracer, for mass bins in the range $13.25 < \log(M_{200, \text{true}}/M_{\odot}) < 14.5$ (the shaded region in Fig. 6).

which is seen in the gradient image. The central regions appear to be relatively uninformative, in agreement with the conclusions of Ntampaka et al. (2018). For the Compton γ images, the DD gradient images also pick up the outskirts

of the cluster, though without the fine granularity seen in the X-ray tracers.

Gaussian Mask: A somewhat complimentary approach to interpreting the CNN performance is to examine the predicted mass when selected regions of the image are masked. For this study, we define a Gaussian mask in the

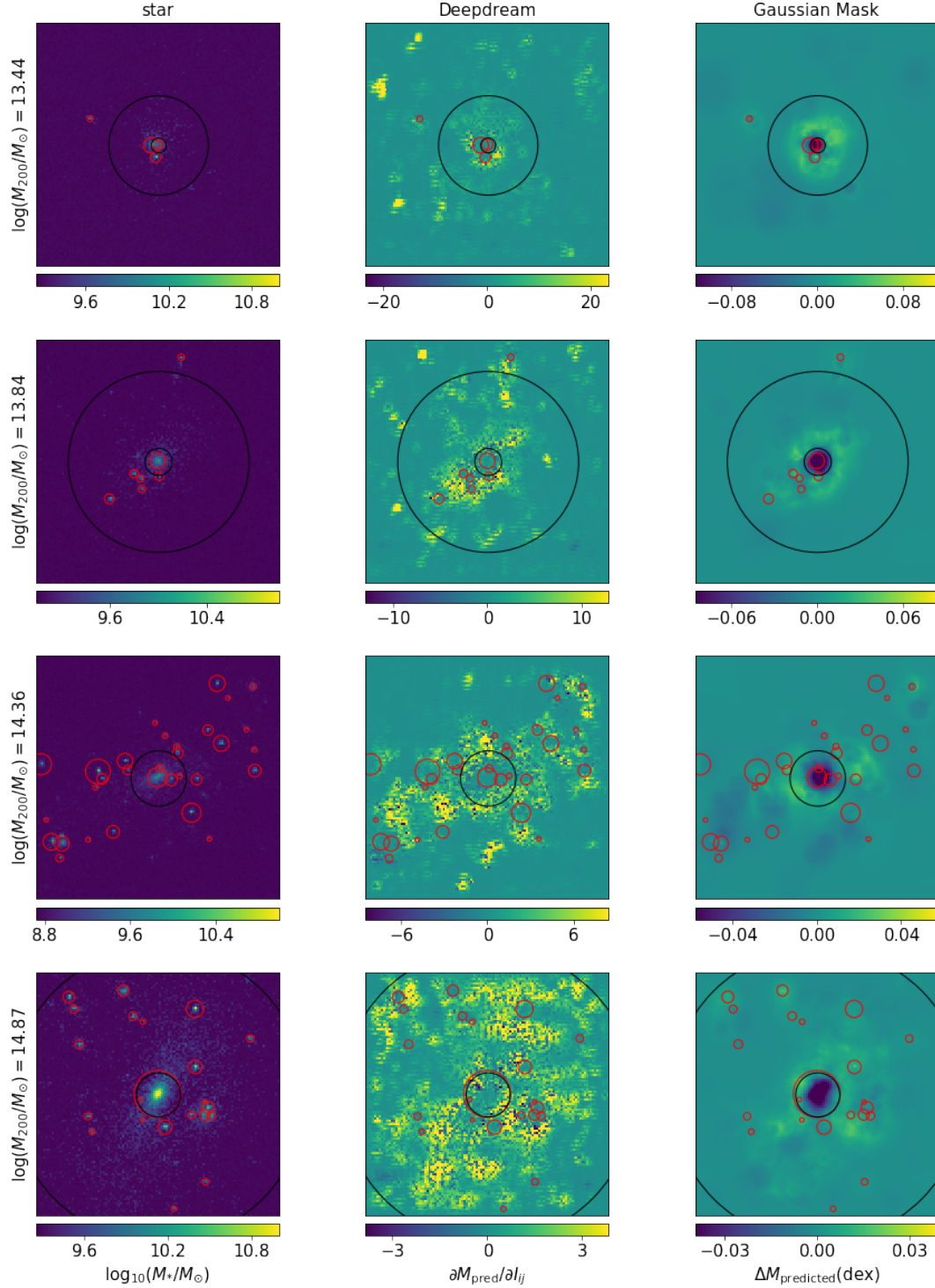


Figure 8. *Left column:* stellar mass images of 4 galaxy clusters selected to cover our mass range; *middle column:* the relative signal change, $\propto \Delta M_{\text{pred}}$, after two Deep Dream iterations; *right column:* the signal change, ΔM_{pred} , when masking the image with a Gaussian mask centered, in turn, on each image pixel (see text for details). The inner black circles indicate $0.15R_{200}$, while the outer circles indicate R_{200} . The red circles highlight galaxy positions, with radii that are proportional to the galaxy’s mass.

image plane as

$$\text{Mask}_{ij} = 1 - \exp \left[-\frac{(i-a)^2 + (j-b)^2}{2\sigma^2} \right], \quad (13)$$

where a and b define the centre of the mask in pixel coor-

dinates, and we take $\sigma = 5$ pixels, corresponding to 1.25 arcmin for our images. For each a and b in the image plane, we multiply the original image by this mask, then use the pre-trained CNN to (re)predict the cluster mass, $M_{\text{pred}}(a, b)$. The results of this test are presented in the right column

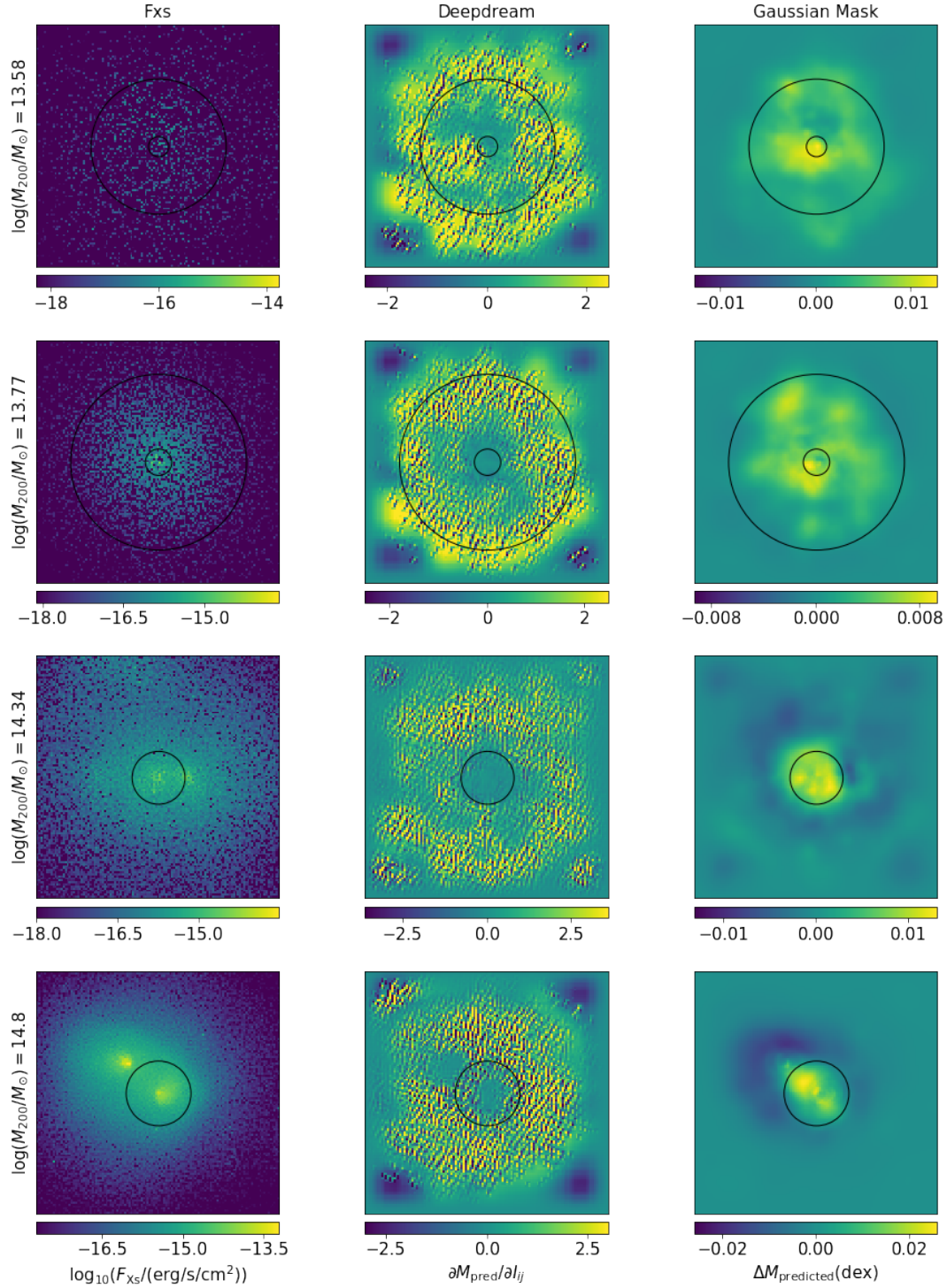


Figure 9. Left column: soft X-ray images of 4 galaxy clusters; middle column: change of signal after two Deep Dream iteration; right column: change of mass prediction when masking the image with Gaussian masks centered at each pixels. The inner circles shows the radius of $0.15R_{200}$ and the outer circles R_{200}

of Figures 8–11, in the form of images of $\Delta M_{\text{pred}}(a, b)$, the change in predicted mass when pixels in the neighbourhood of (a, b) are masked. Pixels that contribute significantly to the original mass estimate will produce a negative ΔM when masked.

For the stellar images, masking the central galaxy re-

duces the predicted mass dramatically, as we might expect. Beyond the central galaxy, the effects are much less clear. There is some mild anti-correlation between the masked image and the DD image, as we might expect, but these are lower level effects compared to the central region.

For the X-ray-based tracers, the mask analysis shows

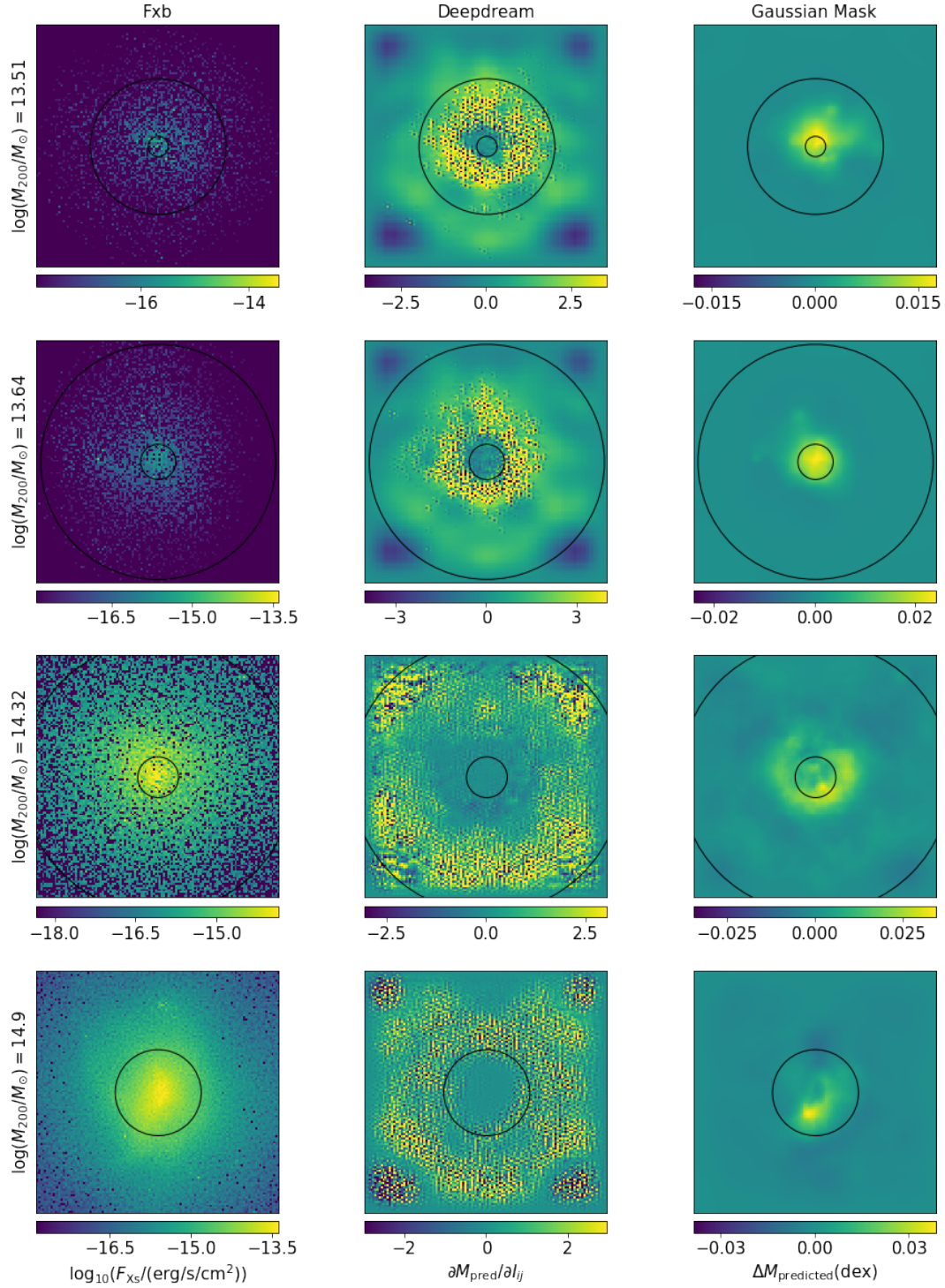


Figure 10. Left column: bolometric X-ray images of 4 galaxy clusters; middle column: change of signal after two Deep Dream iteration; right column: change of mass prediction when masking the image with Gaussian masks centered at each pixels. The inner circles shows the radius of $0.15R_{200}$ and the outer circles R_{200}

that the outskirts of the X-ray data, where the signal gradient is largest, appears to be the most decisive feature the CNN triggers on. As with the DD analysis, the central regions seems to be relatively uninformative. We attribute this to the observation that the signal in the central region is more scattered with respect to cluster mass. We quantify

this by calculating the correlation between the true mass and F_{cent} on the one hand, and F_{ring} on the other, where F_{cent} is the integrated X-ray signal in the range $r < 0.15R_{200}$ and F_{ring} is the integrated signal in the range $0.15R_{200} < r < R_{200}$. The former has a correlation coefficient of 0.58 while the latter is 0.94 (for both Fxs and Fxb).

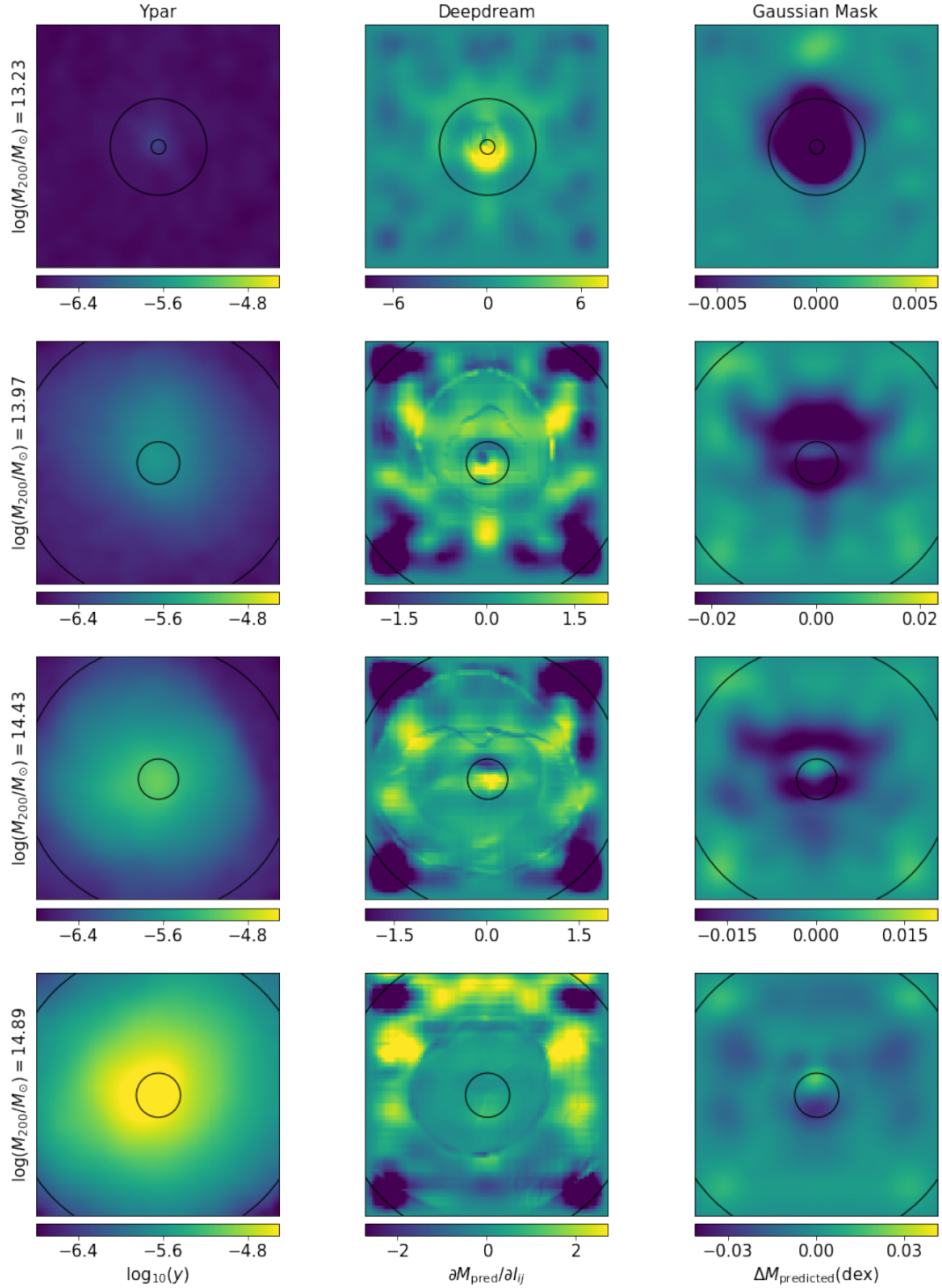


Figure 11. Left column: y parameter images of 4 galaxy clusters; middle column: change of signal after two Deep Dream iteration; right column: change of mass prediction when masking the image with Gaussian masks centered at each pixels. The inner circles shows the radius of $0.15R_{200}$ and the outer circles R_{200}

The Gaussian masked images for the Compton y parameter are more difficult to interpret.

5 CONCLUSION

We construct and train a set of convolutional neural networks (CNNs) to predict galaxy cluster masses, and test the network using a cluster catalogues derived from the BAHAMAS hydrodynamical simulations. The clusters used in

our study range in mass from $10^{12.7}$ to $10^{14.8} M_{\odot}$. Using the simulation database, we generate mock data sets of stellar mass, soft X-ray flux, bolometric X-ray flux, and Compton y -parameter images as input, and train 4 single-channel networks on each of these observables independently. Each network has 3 convolutional layers and 3 pooling layers for feature extraction, followed by 5 fully-connected layers. We also construct a multi-channel network that takes all 4 data sets as simultaneous input. The multi-channel network is configured to run the 4 single-channel feature extraction sections independently. The output is then concatenated and processed by 6 fully-connected layers. We train each network with 6400 randomly-selected cluster images and validate our training using ~ 1600 test images.

Our results are presented in §3. All 5 of the networks successfully learn to predict cluster masses from mock data images. In the mass range $10^{13.25} M_{\odot} < M < 10^{14.5} M_{\odot}$, our networks predict the true mass with a mean bias that is of order of 1%. Outside of this range, our networks tend to over-predict the mass of low-mass clusters and under-predict the mass of high-mass clusters, which is likely due to a bias in the prior distribution of true cluster masses. The per-cluster *rms* scatter is $\sim 15\%$, with the Compton y parameter and the multi-channel networks giving modestly lower scatter than the rest. This performance is better than X-ray and tSZ-based analysis like Zhang et al. (2008) and Bleem et al. (2015) while comparable to the weak lensing analysis of real data reported by Umetsu et al. (2014). However, we note that weak lensing profiles bear richer mass information than the tracers we study, and current weak lensing studies focus on higher-mass clusters. Future work applying CNNs to simulated weak lensing images would be needed to make a fairer comparison.

Henson et al. (2016) estimate cluster masses in the BAHAMAS simulation by fitting the weak lensing profiles of all particles with empirical models. They find a comparable mass bias to ours, however, they don't include noise, so the results are not directly comparable.

So we conclude that our method is more accurate than traditional method on the same hydrodynamical simulation, but the precisions do not improve significantly. We also note that the data set in our analysis is still idealised compared to real observational data.

We use two diagnostics to interpret the performance of our trained networks. Both of them aim to identify image features that 'trigger' the network to reach a particular conclusion. The stellar mass CNN clearly detects galaxies and takes them into account when predicting cluster masses. The gas-based CNNs apparently trigger on the shape and alignment of the gas, but the details are elusive. For example, the X-ray-based CNNs treat the cluster outskirts more importantly than the central region (in agreement with Ntampaka et al. (2018)), however, it is not clear *why* they do. Further understanding of these networks is left to future work.

This paper demonstrates a new approach to measuring galaxy cluster masses, a key parameter for understanding the origin and evolution of large scale structure in the universe. We show that a CNN is capable of recovering cluster masses directly from images of observable signals, despite the presence of substructure and noise. Our method does not require a physical model, however, it does require that one be able to simulate realistic clusters and system-

atic measurement errors reliably. Future work might aim to train networks by combining data from different simulations, or even from real data. We caution that neural networks are notoriously difficult to interpret, so future work should aim to better understand the behavior of hidden layers of the network.

ACKNOWLEDGEMENTS

We thank Dr. Shirley Ho, Nayyer Raza, Riley Hill, Dr. Tilman Tröster and Qiufan Lin for fruitful discussions. The calculations were performed on Compute Canada nodes (www.computecanada.ca). AJM received funding from the European Union's Horizon 2020 research and innovation programme under the Marie Skłodowska-Curie grant agreement No. 702971. This work is financially supported by University of British Columbia, NSERC, and CIFAR. This project has received funding from the European Research Council (ERC) under the European Union's Horizon 2020 research and innovation programme (grant agreement No 769130).

REFERENCES

- Abazajian K. N., et al., 2009, *The Astrophysical Journal Supplement Series*, 182, 543
- Aghanim N., et al., 2016, *Astronomy & Astrophysics*, 594, A22
- Allen S. W., Schmidt R. W., Fabian A. C., 2002, *MNRAS*, 334, L11
- Allen S. W., Evrard A. E., Mantz A. B., 2011, *Annual Review of Astronomy and Astrophysics*, 49, 409
- Bahé Y. M., McCarthy I. G., King L. J., 2012, *MNRAS*, 421, 1073
- Banerji M., et al., 2010, *Monthly Notices of the Royal Astronomical Society*, 406, 342
- Baron D., 2019, arXiv preprint arXiv:1904.07248
- Becker M. R., Kravtsov A. V., 2011, *ApJ*, 740, 25
- Bleem L., et al., 2015, *The Astrophysical Journal Supplement Series*, 216, 27
- Borgani S., Kravtsov A., 2011, *Advanced Science Letters*, 4, 204
- Cohn J., Battaglia N., 2019, arXiv preprint arXiv:1905.09920
- Gitti M., Brighenti F., McNamara B. R., 2012, *Advances in Astronomy*, 2012
- Hasselfield M., et al., 2013, *The Astrophysical Journal Supplement Series*, 209, 17
- Henson M. A., Barnes D. J., Kay S. T., McCarthy I. G., Schaye J., 2016, *Monthly Notices of the Royal Astronomical Society*, p. stw2899
- Hinshaw G., et al., 2013, *ApJS*, 208, 19
- Hinton G., Srivastava N., Swersky K., 2012, *Neural Networks for Machine Learning*, 575
- Hoekstra H., Herbonnet R., Muzzin A., Babul A., Mahdavi A., Viola M., Cacciato M., 2015, *Monthly Notices of the Royal Astronomical Society*, 449, 685
- Lanusse F., Ma Q., Li N., Collett T. E., Li C.-L., Ravanbakhsh S., Mandelbaum R., Póczos B., 2017, *Monthly Notices of the Royal Astronomical Society*, 473, 3895
- Leauthaud A., et al., 2011, *The Astrophysical Journal*, 744, 159
- McCarthy I. G., Schaye J., Bird S., Le Brun A. M. C., 2017, *MNRAS*, 465, 2936
- McCarthy I. G., Bird S., Schaye J., Harnois-Deraps J., Font A. S., van Waerbeke L., 2018, *MNRAS*, 476, 2999
- Melin J.-B., Bartlett J. G., 2015, *A&A*, 578, A21
- Mordvintsev A., Olah C., Tyka M., 2015, Google Research, 2
- Nagai D., Lau E. T., 2011, *The Astrophysical Journal Letters*, 731, L10

- Ntampaka M., et al., 2018, arXiv preprint arXiv:1810.07703
- Planck Collaboration et al., 2016, *A&A*, 594, A24
- Pratt G. W., Croston J. H., Arnaud M., Böhringer H., 2009, *A&A*, 498, 361
- Ribli D., Pataki B. Á., Csabai I., 2019, *Nature Astronomy*, 3, 93
- Rodríguez A. C., Kacprzak T., Lucchi A., Amara A., Sgier R., Fluri J., Hofmann T., Réfrégier A., 2018, *Computational Astrophysics and Cosmology*, 5, 4
- Schaye J., et al., 2010, *MNRAS*, 402, 1536
- Shan H., et al., 2012, *ApJ*, 748, 56
- Simonyan K., Zisserman A., 2014, arXiv preprint arXiv:1409.1556
- Smith G. P., et al., 2016, *MNRAS*, 456, L74
- Sun M., Voit G. M., Donahue M., Jones C., Forman W., Vikhlinin A., 2009, *ApJ*, 693, 1142
- Umetsu K., 2010, arXiv e-prints, p. arXiv:1002.3952
- Umetsu K., et al., 2014, *The Astrophysical Journal*, 795, 163
- Voit G. M., 2005, *Reviews of Modern Physics*, 77, 207
- Yan Z., Raza N., Van Waerbeke L., Mead A., McCarthy I., Tröster T., Hinshaw G., 2020, *Monthly Notices of the Royal Astronomical Society*, 493, 1120
- Zhang Y.-Y., Finoguenov A., Böhringer H., Kneib J.-P., Smith G., Kneissl R., Okabe N., Dahle H., 2008, *Astronomy & Astrophysics*, 482, 451
- Zu Y., Mandelbaum R., 2015, *Monthly Notices of the Royal Astronomical Society*, 454, 1161
- The Chandra Proposers' Observatory Guide, <https://cxc.harvard.edu/proposer/POG/html/index.html>
- von der Linden A., et al., 2014, *Monthly Notices of the Royal Astronomical Society*, 439, 2

This paper has been typeset from a \LaTeX file prepared by the author.